JOURNAL OF GUIDANCE, CONTROL, AND DYNAMICS
Vol. 34, No. 4, July–August 2011

Artificial-Immune-System-Based Aircraft Failure Evaluation over Extended Flight Envelope

Hever Moncayo,* Mario G. Perhinschi,† and Jennifer Davis*
West Virginia University, Morgantown, West Virginia 26508

DOI: 10.2514/1.52748

This paper describes the design, development, and flight-simulation testing of an artificial-immune-system-based approach for the evaluation of different aircraft subsystem failures/damages. The evaluation consists of the estimation of the magnitude/severity of the failure and the prediction of the achievable states, leading to an overall assessment of the effects of the failure on reducing the flight envelope. A supersonic fighter model is used, which includes model-following adaptive control laws based on nonlinear dynamic inversion and artificial neural network augmentation. Data collected from a motion-based flight simulator were used to define the self for a wide area of the flight envelope and to test and validate the proposed approach. Example results are presented for failure-magnitude evaluation and flight-envelope-reduction prediction for abnormal conditions affecting sensors, actuators, engine, and wing structure. Successful failure detection and identification are assumed before evaluation. The results show the capabilities of the artificial-immune-system-based scheme to evaluate the severity of the failure and to predict the reduction of the flight envelope in a general manner.

Nomenclature

C = set of constraints
c_i = flight-envelope estimator center
DNN = decentralized set of neural networks
DQEE_x = decentralized quadratic estimation error
F_k = failure number k
MNN = main set of neural networks
MQEE = main quadratic estimation error
N = total number of features
N_F = total number of failures
N_S = total number of clusters
$\mathrm{NN}_{\mathrm{out}x}$ = specific neural network output
OQEE = output quadratic estimation error
p, q, r = measured roll, pitch, and yaw rate, rad/s
$\hat{p}_{\mathrm{DNN}}$, $\hat{q}_{\mathrm{DNN}}$, $\hat{r}_{\mathrm{DNN}}$ = neural estimates of angular rates that do not include the respective gyro, rad/s
$p_{f_{\max}}$, $p_{f_{\min}}$ = maximum and minimum roll rate, rad/s
$\hat{p}_{\mathrm{MNN}}$, $\hat{q}_{\mathrm{MNN}}$, $\hat{r}_{\mathrm{MNN}}$ = neural estimates of angular rates that include the respective gyro, rad/s
$q_{f_{\max}}$, $q_{f_{\min}}$ = maximum and minimum pitch rate, rad/s
$r_{f_{\max}}$, $r_{f_{\min}}$ = maximum and minimum yaw rate, rad/s
r_i = flight-envelope estimator radius
S_i = n-dimensional flight-envelope estimators
x_{Fk} = known variables
x_{TE} = angular-rate tracking error, rad/s
$\delta_{a_{\max}}$, $\delta_{a_{\min}}$ = maximum and minimum aileron deflections, deg
$\bar{\delta}_{a_{\max}}$, $\bar{\delta}_{a_{\min}}$ = maximum and minimum normalized-aileron deflections, deg
$\delta_{a/\mathrm{left}_{\max}}$, $\delta_{a/\mathrm{left}_{\min}}$ = maximum and minimum left-aileron deflections, deg
$\delta_{a/\mathrm{right}_{\max}}$, $\delta_{a/\mathrm{right}_{\min}}$ = maximum and minimum right-aileron deflections, deg
δ_{dir} = pedal input
$\delta_{e_{\max}}$, $\delta_{e_{\min}}$ = maximum and minimum stabilator deflections, deg
$\delta_{e/\mathrm{left}_{\max}}$, $\delta_{e/\mathrm{left}_{\min}}$ = maximum and minimum left-stabilator deflections, deg
$\delta_{e/\mathrm{right}_{\max}}$, $\delta_{e/\mathrm{right}_{\min}}$ = maximum and minimum right-stabilator deflections, deg
δ_{lat} = lateral stick input
δ_{lg} = longitudinal stick input
$\delta_{r_{\max}}$, $\delta_{r_{\min}}$ = maximum and minimum rudder deflections, deg
$\delta_{r/\mathrm{left}_{\max}}$, $\delta_{r/\mathrm{Left}_{\mathrm{MIN}}}$ = maximum and minimum left-rudder deflections, deg
$\delta_{r/\mathrm{right}_{\max}}$, $\delta_{r/\mathrm{right}_{\min}}$ = maximum and minimum right-rudder deflections, deg
$\delta_{T_{\max}}$, $\delta_{T_{\min}}$ = maximum and minimum power setting of the engine, %
$\delta_{T/\mathrm{left}_{\max}}$, $\delta_{T/\mathrm{left}_{\min}}$ = maximum and minimum power settings for left engine
$\delta_{T/\mathrm{right}_{\max}}$, $\delta_{T/\mathrm{right}_{\min}}$ = maximum and minimum power settings for right engine

I. Introduction

IN RECENT years, several technologies have been developed to improve postfailure flight safety [1–3]. Most of the research toward this end includes high-performance real-time fault detection and identification (FDI) for different critical aircraft subsystems. The FDI schemes may allow an aircraft to avoid unrecoverable postfailure flight conditions, regain equilibrium, and continue the mission by triggering compensating changes in the control laws. It is also important to develop approaches for assessing the severity and the impact of those abnormal conditions on the degradation of performance and the limitation to accomplish specific missions. Information regarding the occurrence of the failure, location, magnitude, and effect on reducing the flight envelope are necessary for the pilot and the control system. The existence of a fault detection, identification, and evaluation (FDIE) scheme can support automatic accommodation as part of a fault-tolerant control system and it can also improve human accommodation through increased pilot situational awareness.

A variety of research efforts have been conducted in the past few years on the development of envelope estimation and protection

---

Presented as Paper 2010-8038 at the AIAA Guidance, Navigation, and Control Conference, Toronto, Canada, 2–5 August 2010; received 12 October 2010; revision received 27 January 2011; accepted for publication 24 February 2011.

*Graduate Student, Department of Mechanical and Aerospace Engineering.

†Associate Professor, Department of Mechanical and Aerospace Engineering. Senior Member AIAA.

methodologies for aircraft under damage/failure conditions. Techniques based on obstacle avoidance for prediction of envelope violation have been proposed [4,5]. The control/command margins are estimated by forcing a set of limit parameters to track an adaptive safe trajectory near the limit boundary. These approaches have been successfully implemented within a nonlinear simulation environment and tested for load factor envelope protection [5]. Adaptive flight-envelope estimation based on online learning neural networks has also been investigated [6]. The approach was demonstrated with NASA's Generic Transport Model, in which the command limits of the controller were constantly adapted to allow the aircraft to fly close to its limit boundary under actuator failures. Alternative approaches have used analytical methods to identify the aerodynamic performance degradation and its impact on the dynamic flight envelope [7]. These were demonstrated for different lifting-surface-damage scenarios. Despite successful designs for individual FDI problems at specific flight regimes, an integrated and comprehensive solution for all subsystem over the entire flight envelope, including complete failure evaluation, is still to be developed. An integrated set of methodologies [8] for detection and identification of a wide variety of aircraft subsystem failures/damages has been designed and implemented at West Virginia University (WVU) within NASA's Aviation Safety Program based on the artificial immune system (AIS) paradigm. As part of this research effort, an integrated high-performance AIS-based FDI scheme using a hierarchical multiself (HMS) strategy has been developed [9]. The scheme is capable of detecting and identifying several categories of subsystem abnormal conditions over an extended area of the flight envelope. The general aspects of the aircraft subsystem FDI scheme, including the additional evaluation phase, are illustrated in Fig. 1 [8].

In this paper, a novel approach for assessing the severity of the failure and estimating the performance limits based on the AIS for several types of failures is proposed. In general, the failure-evaluation process must address distinct aspects such as determining the type of the failure and its magnitude or severity and evaluating the reduction of the flight envelope due to the failure, in the most comprehensive sense. Evaluation requires the previous correct detection and identification of the anomalous conditions. These two aspects are important to diagnose the effect of the failure on the aircraft operational limits and provide necessary information to the pilot and the automatic control system to avoid commands that might lead to loss of control and other dangerous/catastrophic situations. The proposed approach is envisioned as a part of an integrated and comprehensive potential solution to the aircraft FDIE problem.

The general aspects of the proposed AIS-based fault-evaluation approach are presented in Sec. II. The simulation environment, including aircraft subsystem-failure modeling and motion-based flight-simulator tests for self definition and evaluation testing, is presented in Sec. III. Sections IV and V provide details on the design and implementation of the fault-evaluation schemes. In these sections, the functionality of the proposed approach is illustrated through some results and analysis. Finally, the conclusions are summarized in Sec. VI.

II. AIS-Based Fault-Evaluation Approach

A. Artificial Immune System

The AIS emerged in recent years as a new computational paradigm in artificial intelligence. The concept has shown a very promising potential for a variety of applications, such as anomaly detection, data mining, computer security, adaptive control, and pattern recognition.

The immunity-based fault detection [10–12] operates similarly to the biological immune system, according to the principle of self–nonself discrimination, when it detects microbial and nonmicrobial exogenous antigens while not reacting to the self cells. T-cells are the components of the system with the most important role in this process [13]. T-cells are first generated through a pseudorandom genetic-rearrangement mechanism, which ensures high variability of the new cells in terms of biological features (typically, proteins or polysaccharides). A censoring process then takes place in the thymus (Fig. 2), resulting in the destruction of the T-cells that react against self proteins. Eventually, only those T-cells that do not bind to self proteins are allowed to leave the thymus, proliferate, or produce copies (clones) of themselves. For obvious reasons, this process is referred to as negative selection (NS) [14–17]. The matured T-cells (antibodies or detectors) can circulate throughout the body to detect antigens and mark them for destruction (Fig. 2). As an alternative mechanism, positive selection (PS) [18,19] has been explored for AIS design. Through the positive-selection strategy, the detectors are generated to coincide with the self, and the process is equivalent to clustering the self data. In this case, an abnormal situation is declared

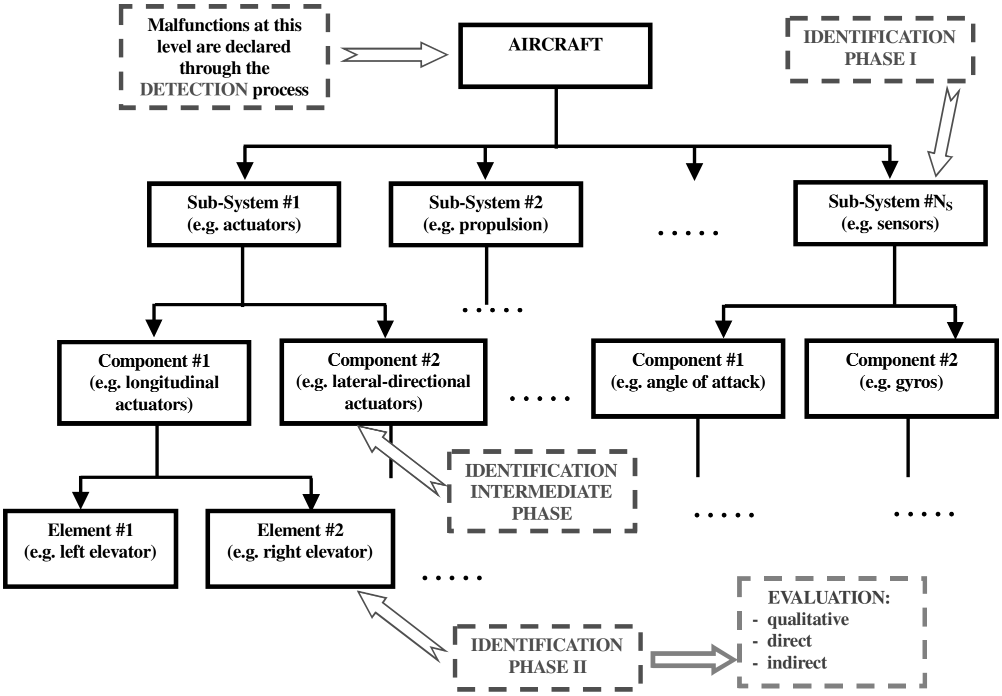

Fig. 1 Aircraft subsystem FDIE scheme

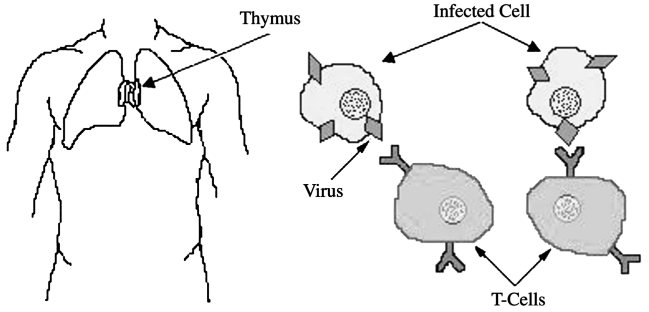

Fig. 2 Generation of T-Cells in the thymus and antigen detection

if the explored current configuration does not match any of the detectors. For detection purposes, NS and PS are equivalent; however, using PS within a detection scheme is typically more computationally intensive than using NS because it is necessary to test the complete set of positive antibodies before classifying a sample as abnormal. With the NS approach, the activation of a single negative antibody is enough to declare the presence of an abnormal situation. For the identification and evaluation phases, additional information is needed to structure the nonself hyperspace, which can be obtained through a PS type of mechanism using data under failure conditions. In particular, for the quantitative direct evaluation, the nonself must be separated into subregions corresponding to the different identifiable level of failures and PS must be used to assess the distribution of the failure signature within the nonself by labeling the antibodies corresponding to different magnitudes of the failure.

B. Fault Evaluation

In previous research efforts, the AIS has been demonstrated to be successful for fault detection and identification of aircraft subsystems failures by using the HMS strategy [9]. The HMS has the merit of significantly improving the detection performance with reduced computational requirements relying on an integrated multiple self approach instead of considering single self configurations. Once a failure has been detected and correctly identified, the evaluation phase is intended to addresses three aspects. One is of a qualitative nature and involves determining the type of the failure. For example, the qualitative evaluation is expected to determine if an actuator failure consists of a locked actuator, or a freely moving control surface, or a reduction of control efficiency. The qualitative aspect can be determined by considering the type of failure as an additional classification target and treating it similarly to an additional identification phase. However, this type of failure evaluation has not been addressed in this paper. The other two aspects are of a quantitative nature and can be defined as direct and indirect. Both these aspects have been addressed within this paper. The direct failure evaluation consists of estimating the magnitude or severity of the failure (e.g., left aileron locked at +10 deg). The indirect failure evaluation includes the reassessment of the flight envelope and prediction of the limitations and constraints on the performance and handling qualities inflicted by the presence of the failure.

Consistent design algorithms have been proposed for detection and identification [8,9] that can be applied to a variety of systems and abnormal condition types without changes. The failure-evaluation process may require additional customization depending on the subsystem, failure, and affected parameter of the flight envelope addressed by the evaluation.

The direct evaluation or failure-magnitude assessment can be approached at three levels of accuracy. An approximate magnitude assessment, using larger categories such as small, medium, and large, can be performed by considering an additional classification target within each identified abnormal condition. This process is performed based on the distance of every single activated identifier with respect to a previously defined self. Figure 3 illustrates a typical failure signature in a two-dimensional space. The hyperspheres represent the identifiers generated through positive selection for that particular failure. Note that failures of high magnitude correspond to points located at larger distances with respect to the self, and failures of low magnitude correspond to points located closer to the self. This hypothesis is based on observations of simulation scenarios of several types of failures affecting the main four subsystems considered within this research effort. In consequence, before a high-magnitude identifier is activated, low-magnitude identifiers have already been activated, resulting in a certain reduction of the evaluation rate for high magnitude of failures or a delay in the evaluation. Higher-accuracy quantitative magnitude assessment with numerical outcomes is possible based on a combination of AIS algorithms and analytical estimates, provided that extensive experimental data are available.

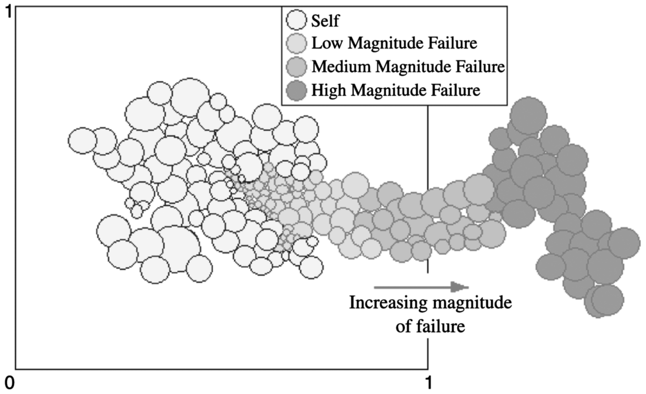

Fig. 3 Signature of failure of different magnitudes in two-dimensional space

The indirect evaluation or reduced flight-envelope prediction must rely on a combined strategy based on analytical flight-envelope-reduction assessment and AIS-based approaches for parameter space reduction assessment. In this paper, a general meaning is attributed to the flight envelope, which includes all dynamic parameters and states that are of interest for performing specific piloting tasks and accomplishing specific missions. However, only a few such parameters will be discussed here. The analytical methods require accurate modeling of the failures and significant online computational capabilities. The AIS method implies that all pertinent parameters to the flight envelope, considering its generalized meaning, are part of the feature sets [8]. Assume that the self is defined as the set of all n-dimensional hyperspheres Si (or flight-envelope estimators) characterized by the center c_i and the radius r_i:

$$S = \{(c_i, r_i)\} = \{S_i\}, \qquad i = 1, 2, \ldots, N_S \tag{1}$$

$$c_i = [x_1, \quad x_2, \quad \ldots, \quad x_n]_i^T \tag{2}$$

where N_S is the total number of clusters and n is the total number of features x_i that define the self. The self can be viewed as a generalized flight envelope based on parameters x_i. Assume that each failure F_k is defined by a set of constraints C on known variables x_{Fk}, with $k = 1, 2, \ldots, N_F$:

$$C = C(x_{Fk}) \tag{3}$$

The variables x_{Fk} must be part of the feature set:

$$\{x_{Fk}\}_{k=1,2,\ldots,N_F} \subset \{x_j\}_{j=1,2,\ldots,n} \tag{4}$$

Then a new self or reduced envelope as a consequence of F_k can be defined as

$$S_{\text{new}} = \{(c_i, r_i) | (c_i, r_i) \Leftarrow C(x_{Fk})\} \tag{5}$$

The proposed approach for indirect evaluation requires that the direct evaluation is successful and that the effects of the failure can be related to constraints on at least one variable in the feature set. Then the effects on other variables in the feature set can be evaluated. The concept is illustrated in Fig. 4 for the two-dimensional case. The novelty in this approach is the use of AIS for online estimation of

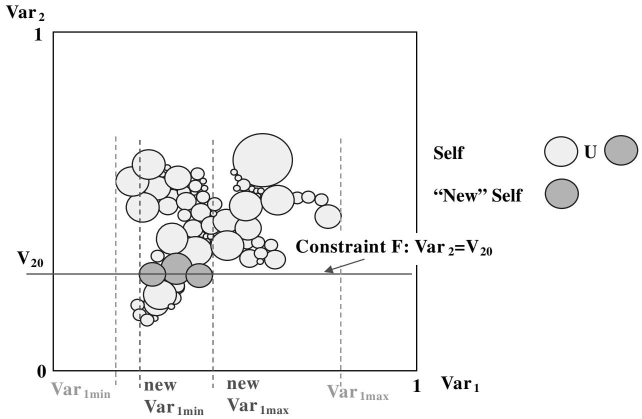

Fig. 4 Indirect failure evaluation using the AIS paradigm [8].

the achievable flight envelope of the aircraft after occurrence of faults providing an integrated solution with multidimensional capabilities. The output information obtained from this phase will be useful for determining the best compensation tasks within the control laws to avoid dangerous flight conditions due to the failures.

To reduce the computational requirements and improve efficiency, the system is trained offline with the generation of a bank of flight-envelope estimators for the known failures at different possible magnitudes. Then the bank is used for flight-envelope estimation in real time by simple interpolation from the offline-generated library.

III. Simulation Environment and Experimental Setup

A. Aircraft Model

A customized WVU Intelligent Flight Control System (IFCS) F-15 [20] aircraft model was used for this research effort. The aircraft model is derived from a high-performance military aircraft model distributed by NASA to academic institutions in 1990 [21]. The Flight Dynamics and Control MATLAB toolbox provides the general frame for solving the equations of motion. The generic model was customized through the addition of the aerodynamic modeling of canard surfaces for the purpose of simulating the NASA IFCS F-15 research aircraft. Detailed modeling of several types of actuators, sensors, propulsion system, and structural failures/damages has been included.

B. Description of the Failure Modeling

Four types of failures were modeled to support the development and testing of the failure-evaluation scheme: actuator, sensor, propulsion, and structural failures/damages. A brief description of the modeling approach is presented next.

1. Actuator-Failure Modeling

Within this effort, failure on left or right individual stabilators, ailerons, or rudders have been considered, since the aircraft considered is equipped with a dual fin. Two types of control-surface failure are modeled: stuck aerodynamic control surface and physically damaged aerodynamic control surface. The first failure type corresponds to an actuator mechanism failure and results in a locked surface; in fact, at the failure occurrence, the control surface remains fixed in the current position/deflection or moves to a predefined position and remains fixed there. A failure involving a blockage of the control surface at a fixed deflection does not alter the aerodynamic properties of the control surface. However, each surface in a pair (left and right) will have different deflections, and the resulting moments and forces are computed individually. The second failure type corresponds to a physical destruction and/or deformation of the control surface. It consists of a deterioration of the aerodynamic efficiency of the control surface starting at the moment of failure occurrence. A control failure that involves physical damage of the control surface may alter the aerodynamic properties in manners that can be both qualitative (affecting the nature of the aerodynamic phenomena involved) and quantitative (affecting the magnitude of characteristic parameters). More details and complete models are presented in [20,22].

2. Sensor-Failure Modeling

Failures of the gyros on the three channels have been considered within this effort. The simulated sensor failure implemented consists of an output bias. The transition to the biased sensor output can be instantaneous (step bias) or over a certain transient (drifting bias). Different transients and different sizes of the bias can be defined. Thus, two types of sensor failures are implemented: large step bias (LSB) and large fast-drifting step bias (LFSB) in the angular-rate sensors [22].

3. Aerodynamic Surface-Damage Modeling

For the purpose of this paper, only the damage of the wing is modeled separately. Damages to other aerodynamic surfaces may be considered as failures of the respective actuators (loss of aerodynamic efficiency). A simple model of wing damage is developed considering both aerodynamic and gravimetric effects. The failure type corresponds to a total or partial physical destruction and/or deformation of the wing. Different percent values along the wing, starting from the tip, can be selected as the damage-affected area. Given the wing geometry and configuration of the F-15 aircraft, a wing loss beyond 6% span will totally or partially affect the efficiency of the aileron control surface.

4. Engine-Failure Modeling

Simple models for the following engine failures/malfunctions have been implemented: stuck throttle, thrust runaway, and power/thrust-reduced control efficiency. The stuck-throttle failure implies normal operation of the engine, but no response to power-lever actuation. The thrust-runaway failure models a malfunction of the fuel control system, which causes the increase of the fuel flow to maximum and the increase of the thrust as a result. This is modeled by increasing the throttle to maximum with first-order dynamics and time constant set up by the user. Finally, the power/thrust-reduced control efficiency is modeled by scaling down the throttle input by a constant factor selected by the user. For this paper, only the latter type of engine failure is considered.

The simulated failures tested for the purpose of this paper are outlined in Table 1. The training data set was created by taking all of the data from nominal conditions, and the test data were generated from flight tests with failure. An additional validation set of data at normal conditions was acquired to evaluate the level of false alarms.

C. Flight-Simulator Experiment

The experimental data were generated in the WVU six-degree-of-freedom (6-DOF) motion-based flight simulator interfaced with an external computer on which the customized WVU IFCS F-15 [23]

Table 1 Simulated failures

Failure type	Description
	Actuator
Left or right stabilator	Blockage at 8 and 2 deg
Left or right aileron	Blockage at 8 and 2.5 deg
Left or right rudder	Blockage at 8 and 4 deg
	Sensor LSB and LFSB
Roll	10 and 5 deg/s gyro output
Pitch	10 and 5 deg/s gyro output
Yaw	3 and 1 deg/s gyro output
	Structural damage
Left or right wing	Loss of 15% of wing, affecting the efficiency of the aileron. Loss of 6% of wing, without affecting the efficiency of the aileron
	Power/thrust-reduced control efficiency
Left engine	Loss of 98% and 60% power
Right engine	Loss of 98% and 60% power

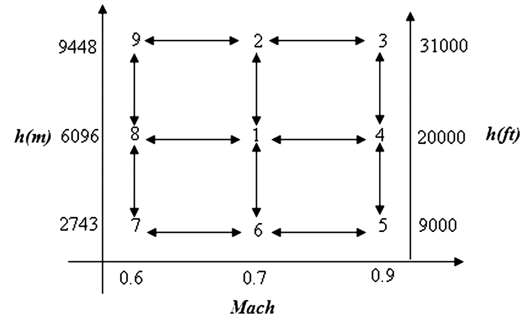

Fig. 5 Testing flight envelope.

research aircraft model was run within the MATLAB/Simulink environment. This experimental setup offers a very realistic flight environment allowing good motion and visual cues.

Different flight scenarios were performed over a wide area of the flight envelope, which was first defined based on nine specific reference points (Fig. 5) for Mach numbers between 0.6 and 0.9 and altitudes between 9000 and 31,000 ft. Flight tests start at the steady-state flight condition 1 and continue to cover the nine points, as described by the arrows in Fig. 5. Data at all flight conditions along the arrows are used to build the self. For example, one flight test starts at point 1, the aircraft is accelerated at constant altitude to point 4, descended at constant speed to point 5, and then returned to points 4 and 1. A total of eight such tests were necessary to cover the testing flight envelope.

The set of flight scenarios, lasting between 10 and 20 min each, are designed to include steady-state flight conditions, transitions between steady-state conditions, and mild-to-moderate maneuvers. These flight scenarios are simulated under normal flight conditions. They are repeated under various failure scenarios for both design/development and validation purposes. Only one failure at a time is considered to capture/isolate the dynamic fingerprint of each type of failure and generate antibodies appropriately. The data from the simulator were acquired at a rate of 50 Hz.

IV. Performance of the AIS-Based Direct Fault-Evaluation Approach

A critical element for the success of the AIS-based direct evaluation scheme is the selection of the appropriate parameters to capture the dynamic signature of the failures. Previous studies have put into evidence promising parameters for FDI [23]. Some of them have been selected for further use within the evaluation phase.

Angular-rate tracking errors x_{TE} on all three channels are

$$x_{\mathrm{TE}} = x - x_{\mathrm{ref}} \tag{6}$$

where $x = p, q$, or r (roll, pitch, or yaw rate) and x_{ref} is the reference rate determined within the model-following control laws directly from pilot input to meet first- or second-order responses as required for good handling qualities. Artificial neural network output $\mathrm{NN}_{\mathrm{out}}$ on all three channels consists of angular accelerations [24,25]. Parameters based on neural network estimates of angular rates [23,26] include the main quadratic estimation error:

$$\begin{aligned}\mathrm{MQEE}(k) = {}&\tfrac{1}{2}[(p(k) - \hat{p}_{\mathrm{MNN}}(k))^2 + (q(k) - \hat{q}_{\mathrm{MNN}}(k))^2\\ &+ (r(k) - \hat{r}_{\mathrm{MNN}}(k))^2]\end{aligned} \tag{7}$$

where $p(k)$, $q(k)$, and $r(k)$ are measurements of angular rates at sample k and $\hat{p}_{\mathrm{MNN}}(k)$, $\hat{q}_{\mathrm{MNN}}(k)$, and $\hat{r}_{\mathrm{MNN}}(k)$ are neural estimates of the angular rates based on sensor measurements including the respective gyro, over a specified time window. A second parameter based on NN estimates is the output quadratic estimation error, defined as

$$\begin{aligned}\mathrm{OQEE}(k) = {}&\tfrac{1}{2}[(\hat{p}_{\mathrm{DNN}}(k) - \hat{p}_{\mathrm{MNN}}(k))^2 + (\hat{q}_{\mathrm{DNN}}(k) - \hat{q}_{\mathrm{MNN}}(k))^2\\ &+ (\hat{r}_{\mathrm{DNN}}(k) - \hat{r}_{\mathrm{MNN}}(k))^2]\end{aligned} \tag{8}$$

where $\hat{p}_{\mathrm{DNN}}(k)$, $\hat{q}_{\mathrm{DNN}}(k)$, and $\hat{r}_{\mathrm{DNN}}(k)$ are neural estimates of the angular rates based on sensor measurements that do *not* include the respective gyro, over a specified time window. Finally, the decentralized quadratic estimation error parameter is also used for detection:

$$\mathrm{DQEE}_x(k) = \tfrac{1}{2}(\hat{x}_{\mathrm{DNN}}(k) - x(k))^2, \qquad x = p, q, r \tag{9}$$

The three configurations of features outlined in Table 2 were selected to generate hyperspherical identifiers [27] corresponding to each type of failure through a positive-selection process. Then they were integrated into the HMS to improve the activation performance.

To perform the direct evaluation phase, several failure magnitudes have been considered. Using the concept of identifiers, a classification based on wide categories such as small, medium, and large was performed. The ranges of these classifiers were established based on the observed sensitivity of the aircraft response and are specified in the column headings of Tables 3–7. Figures 6 and 7 present two-dimensional examples of signatures for high-magnitude stabilator and sensor failures, respectively. Note the distribution of the failure data in the nonself space (even outside of the unit hypercube). This favors the classification of different levels of magnitude for each failure. Tables 3–7 present the results of the direct evaluation performance of the HMS for the four categories of failures considered: actuator, sensor, structural, and propulsion system.

The evaluation rates listed in Tables 3–7 represent percentages of all data samples that have been declared to be the result of a failure of a specific magnitude/severity. For example, tests with the left rudder locked at 4 deg have yielded the following results. 2.38% of the samples were evaluated to be the result of a low-severity failure, 97.61% were evaluated to be the result of a medium severity failure, and 0% were evaluated as a high-severity failure. A low-severity

Table 2 Feature configurations for self definition

Self number	Features	Solution space dimension
Self 1	$\mathrm{NN}_{\mathrm{out}x}$ and DQEE_x	6
Self 2	$\mathrm{NN}_{\mathrm{out}x}$ and x_{TE}	6
Self 3	$\mathrm{NN}_{\mathrm{out}x}$, MQEE, OQEE, and DQEE_x	8

Table 3 Actuator failure

Failure type	Failure category (evaluation rates, %) Low 2 ± 1.5 deg	 Medium 5 ± 1.5 deg	 High 8 ± 1.5 deg
2 deg, left stabilator	99.15	0.84	0
8 deg, left stabilator	2.00	16.85	81.14
2 deg, right stabilator	95.10	4.89	0
8 deg, right stabilator	1.20	11.54	87.24
2.5 deg, left aileron	100	0	0
8 deg, left aileron	4.08	11.27	84.63
2.5 deg, right aileron	98.57	1.43	0
8 deg, right aileron	4.36	9.51	86.11
4 deg, left rudder	2.38	97.61	0
8 deg, left rudder	0	0	100
4 deg, right rudder	0	100	0
8 deg, right rudder	0	0	100

Table 4 Sensor failure

Failure type	Failure category (evaluation rates, %) Low 2 ± 1 deg/s	 Medium 5 ± 2 deg/s	 High 9 ± 2 deg/s
5 deg/s, p: LSB	0	100	0
10 deg/s, p: LSB	0	0.35	99.64
5 deg/s, q: LSB	0	100	0
10 deg/s, q: LSB	0	0	100

Table 5 Sensor failure

Failure type	Failure category (evaluation rates, %)		
	Low	Medium	High
	1 ± 0.5 deg/s	2 ± 0.5 deg/s	3 ± 0.5 deg/s
1 deg/s, r: LSB	100	0	0
3 deg/s, r: LSB	0.29	0.38	99.31

Table 6 Structural failure

Failure type	Failure category (evaluation rates, %)		
	Low	Medium	High
	$6 \pm 2.5\%$	$11 \pm 2.5\%$	$16 \pm 2.5\%$
6%, left wing	100	0	0
15%, left wing	0.05	7.78	92.15
6%, right wing	100	0	0
15%, right wing	0.74	11.88	87.37

Table 7 Engine failure

Failure type	Failure category (evaluation rates, %)			
	Low	Medium	Medium	High
	$\leq 40\%$	$50 \pm 10\%$	$70 \pm 10\%$	$90 \pm 10\%$
60%, left engine	0	0	100	0
98%, left engine	0	0	0	100
60%, right engine	0	0	100	0
98%, right engine	0	0	0	100

failure is assumed if the locked deflection is between 0.5 and 3.5 deg/s in either direction, a medium severity failure is assumed if the locked deflection is between 3.5 and 6.5 deg/s, and a high-severity failure is assumed if the sensor bias is between 6.5 and 9.5 deg/s. Since the tested failure falls in the medium range, the results of the evaluation can be considered very good. It should be noted that the high percentage of low-severity evaluations is equivalent to a delay in evaluating a higher-severity failure. This aspect could be taken into account by using an evaluation logic considering information over a previous time window for a final failure-evaluation outcome.

The results show that a high direct evaluation rate for different magnitudes of failure in all categories is achieved. For the sensor and engine failures, for example, the percent of evaluation rate achieves even 100%. Good performance is also achieved for the structural and actuator failures; however, as explained in Sec. II, the apparent better performance obtained for low-magnitude cases is due to the natural migration of the data points away from the self, passing first through regions of the hyperspace that correspond to low-magnitude failures. If this data migration takes place faster, then the evaluation rate for the higher-severity cases increases. This migration rate could be a good indicator for evaluation and this hypothesis should be investigated in the future.

V. Performance of the AIS-Based Indirect Fault-Evaluation Approach

According to the criteria described in Sec. II, the indirect evaluation process has been implemented within the HMS scheme. Once a failure is detected, identified, and its magnitude correctly determined, the achievable operational limits of the aircraft can be estimated based on all or some dynamic parameters and states that are important to accomplish specific pilot tasks or missions.

For every category of failure, a set of relevant parameters defining the performance limits of the aircraft has been selected. Then hypersphere evaluators are generated and their capabilities to predict the reduction of the flight envelope are analyzed.

A. Control-Surface Failure

For control-surface failures, the angular rates in all three channels have been considered to be part of the feature sets that define the self. Corresponding control-surface deflections under abnormal conditions will produce constraints and alteration/reduction of the possible range of angular rates. Thus, the operational ranges of the aircraft in terms of angular rates can be determined based on the achievable limits of these variables in the presence of control-surface abnormal operation.

Because a certain delay exists between the angular rates and the corresponding control deflections, preprocessing of the data needs to be performed in order to reduce this effect and obtain a more direct relationship between these two sets of variables.

Using healthy flight-test data from the nine points of the flight envelope described in Sec. III, the three angular rates and corresponding deflection variables were plotted and the limits of nominal flight condition obtained. In this paper, a positive differential aileron deflection is assumed to produce positive rolling moment, and a positive elevator and rudder deflection will produce negative pitch and yaw moments, respectively. Since different scales of the variables are not desirable, the data has been normalized between 0 and 1 with respect to the maximum and minimum values of each variable. Therefore, 0 deg of actuator deflection, for example, will

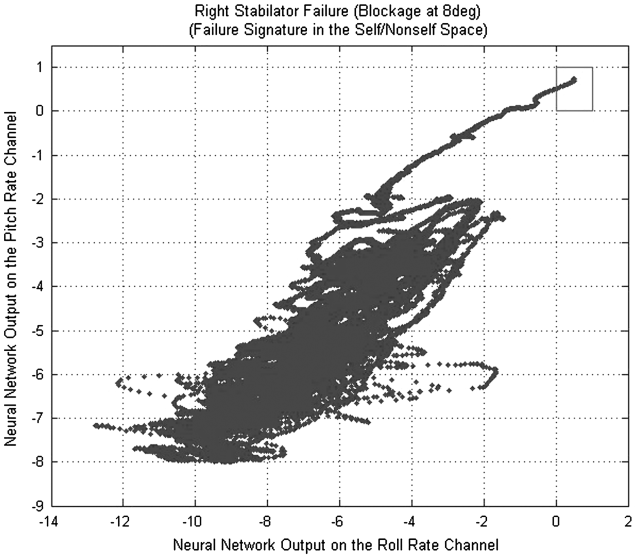

Fig. 6 Signature of a failure in the right stabilator.

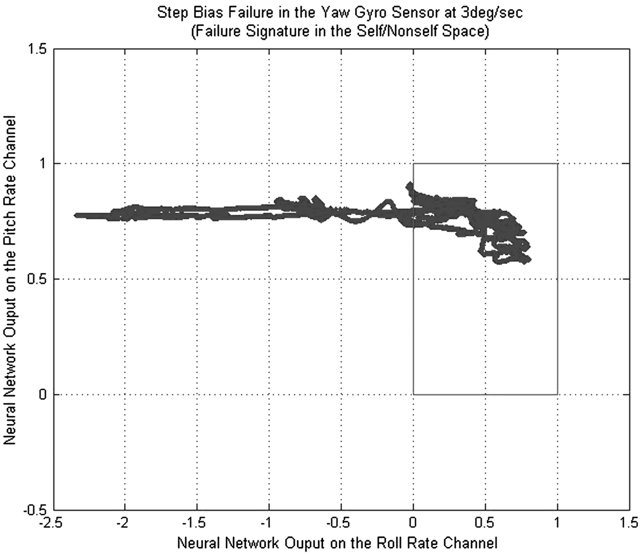

Fig. 7 Signature of a failure in the yaw gyro sensor.

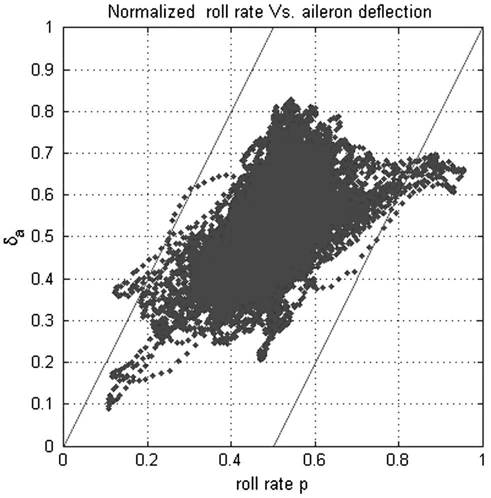

Fig. 8 Defined self for envelope reduction due to aileron failure.

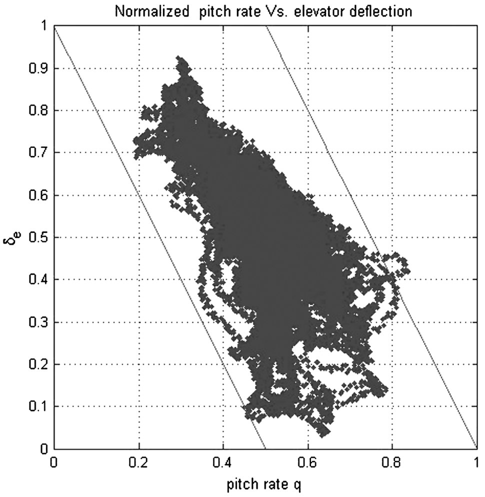

Fig. 9 Defined self for envelope reduction due to stabilator failure

correspond to 0.5 after normalization. Figures 8–10 show 2-D normalized plots of these variables where a 15% margin has been used. This margin is particularly useful when additional sets of nominal data are to be combined with previously acquired/processed sets. The operational ranges are summarized in Table 8.

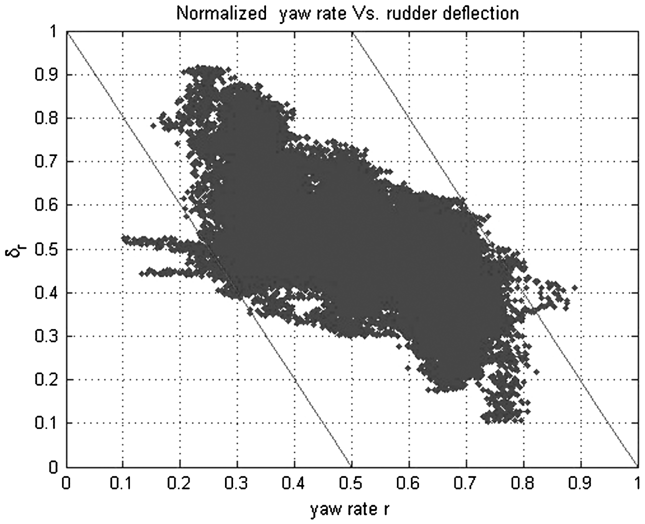

Fig. 10 Defined self for envelope reduction due to rudder failure

Table 8 Nominal operational ranges

Self variable	Minimum nominal limit	Maximum nominal limit
Roll rate	−1.19 rad/s	1.19 rad/s
Aileron deflection	−11 deg	11 deg
Pitch rate	−0.25 rad/s	0.25 rad/s
Stabilator deflection	−8 deg	8 deg
Yaw rate	−0.08 rad/s	0.08 rad/s
Rudder deflection	−24 deg	24 deg

It is important to note that the y axis in Figs. 8–10 represents the total generic deflection of the pair of control surfaces, which is differential for the aileron and collective for stabilator and rudder. For example, assuming a lockage of the left-aileron control surface at 8 deg, the constraint range for the generic aileron deflection can be determined as follows:

$$\delta_{a_{\max}} = \frac{\delta_{a/\mathrm{left}_{\max}} - \delta_{a/\mathrm{right}_{\max}}}{2} = \frac{8\ \mathrm{deg} + 11\ \mathrm{deg}}{2} = 9.5\ \mathrm{deg} \tag{10}$$

$$\delta_{a_{\min}} = \frac{\delta_{a/\mathrm{left}_{\min}} - \delta_{a/\mathrm{right}_{\min}}}{2} = \frac{8\ \mathrm{deg} - 11\ \mathrm{deg}}{2} = -1.5\ \mathrm{deg} \tag{11}$$

where $\delta_{a/\mathrm{left}_{\max}}$ and $\delta_{a/\mathrm{right}_{\max}}$ represent the maximum deflections for left and right ailerons, respectively, and $\delta_{a/\mathrm{left}_{\min}}$ and $\delta_{a/\mathrm{right}_{\min}}$ represent the minimum deflections. These deflections are normalized by mapping the nominal range of Table 8 [−11, 11] deg onto the interval [0, 1]. The normalized values correspond to: $\bar{\delta}_{a_{\max}} = 0.93$ and $\bar{\delta}_{a_{\min}} = 0.43$. Note that within the model, trailing-edge down deflection is assumed to be positive, and the total aileron deflection is defined as the deflection of the left surface minus deflection of the right surface, divided by 2. This is consistent with the way the control derivatives are defined within the model.

Considering the right-stabilator control surface locked at 5 deg, the constraint range for the collective stabilator deflection is determined as

$$\delta_{e_{\max}} = \frac{\delta_{e/\mathrm{left}_{\max}} + \delta_{e/\mathrm{right}_{\max}}}{2} = \frac{8\ \mathrm{deg} + 5\ \mathrm{deg}}{2} = 6.5\ \mathrm{deg} \tag{12}$$

$$\delta_{e_{\min}} = \frac{\delta_{e/\mathrm{left}_{\min}} + \delta_{e/\mathrm{right}_{\min}}}{2} = \frac{-8\ \mathrm{deg} + 5\ \mathrm{deg}}{2} = -1.5\ \mathrm{deg} \tag{13}$$

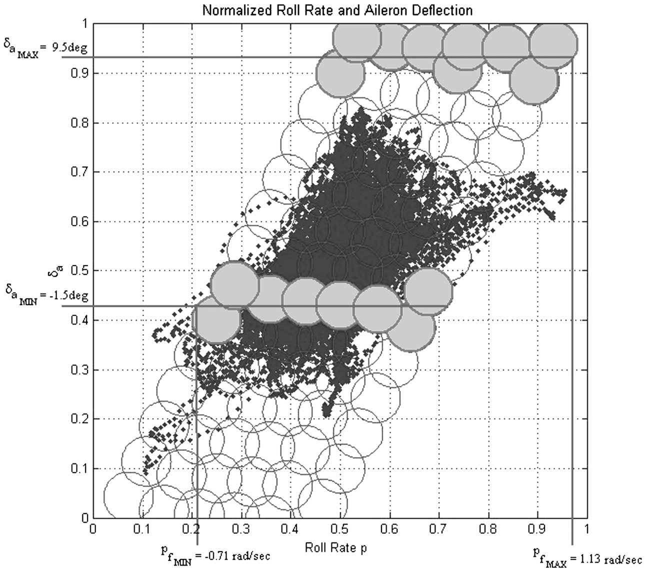

Fig. 11 Evaluator distribution and activation for left-aileron control surface locked at 8 deg

In the case of a left rudder stuck at 4 deg, the constraint range is calculated as

$$\delta_{r_{\max}} = \frac{\delta_{r/\text{left}_{\max}} + \delta_{r/\text{right}_{\max}}}{2} = \frac{4\ \text{deg} + 24\ \text{deg}}{2} = 14\ \text{deg} \tag{14}$$

$$\delta_{r_{\min}} = \frac{\delta_{r/\text{left}_{\min}} + \delta_{r/\text{right}_{\min}}}{2} = \frac{4\ \text{deg} - 24\ \text{deg}}{2} = -10\ \text{deg} \tag{15}$$

After nominal operational limits have been determined, 86 hypersphere evaluators were generated for every self. Figures 11–13 show the distribution of such evaluators filling the defined self regions. As illustration, these figures also present the evaluators that are activated when the considered failure conditions are present. The set of parameters $p_{f_{\max}}$, $p_{f_{\min}}$, $q_{f_{\max}}$, $q_{f_{\min}}$, $r_{f_{\max}}$, and $r_{f_{\min}}$ represent the new maximum and minimum values of the angular rates and define the achievable range under failure condition. Tables 9–11 summarize more results for different magnitudes of control-surface failures. These data can build a bank of estimators for known failures and can be used for flight-envelope estimation in real time.

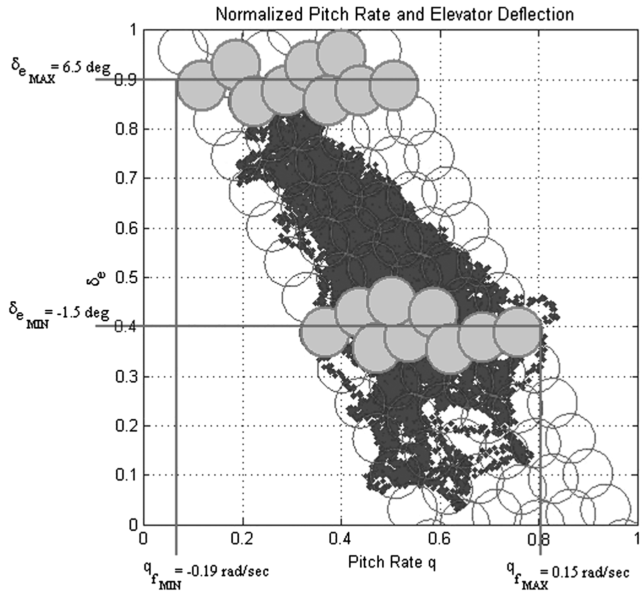

Fig. 12 Evaluator distribution and for right-stabilator control surface locked at 5 deg

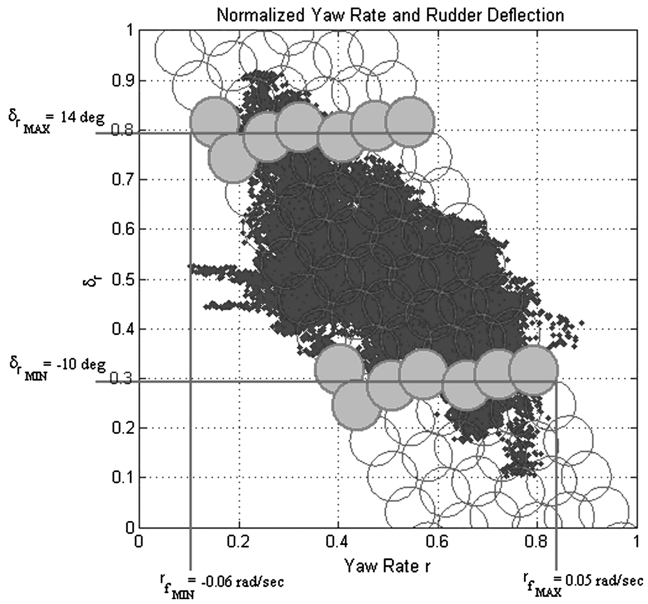

Fig. 13 Evaluator distribution and activation for left-rudder control surface locked at 4 deg

Table 9 Roll- rate failure operational ranges

Failure type	Minimum roll rate $p_{f_{\min}}$, rad/s	Maximum roll rate $p_{f_{\max}}$, rad/s
Left aileron locked at 8 deg	−0.71	1.13
Right aileron locked at 5 deg	−1.05	0.79
Left aileron locked at 2.5 deg	−0.79	0.96
Right aileron locked at 0 deg	−0.88	0.88

Table 10 Pitch-rate-failure operational ranges

Failure type	Minimum pitch rate $q_{f_{\min}}$, rad/s	Maximum pitch rate $q_{f_{\max}}$, rad/s
Left stabilator locked at 8 deg	−0.22	0.12
Right stabilator locked at 5 deg	−0.19	0.15
Left stabilator locked at 2.5 deg	−0.18	0.15
Right stabilator locked at 0 deg	−0.16	0.17

Table 11 Yaw-rate-failure operational ranges

Failure type	Minimum yaw rate $r_{f_{\min}}$, rad/s	Maximum yaw rate $r_{f_{\max}}$, rad/s
Right rudder locked at 16 deg	−0.07	0.04
Right rudder locked at 8 deg	−0.06	0.04
Right rudder locked at 4 deg	−0.06	0.05
Left rudder locked at 0 deg	−0.05	0.06

Finally, to illustrate the performance of the approach, Figs. 14–16 present the signature of the dynamic behavior of the aircraft in terms of angular rates for control-surface-failure conditions. It is clear that the maximum and minimum values for roll, pitch, and yaw rates are inside of the predicted range values determined by the evaluators. This implies that the capabilities of the aircraft performing certain types of maneuvers are limited by the estimated operational ranges in the presence of failures.

B. Sensor Failure

In contrast to the control-surface failures, for the sensor-failure case, the angular rates in all three sensor channels have been considered as a set of constraints that produce maneuvering limits.

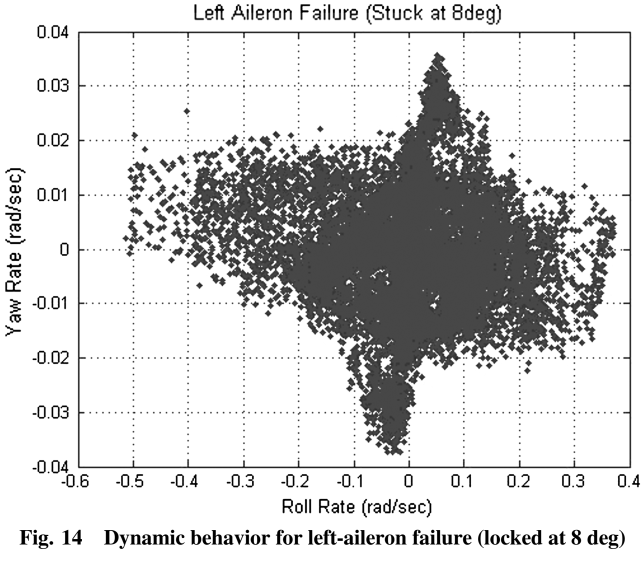

Fig. 14 Dynamic behavior for left-aileron failure (locked at 8 deg)

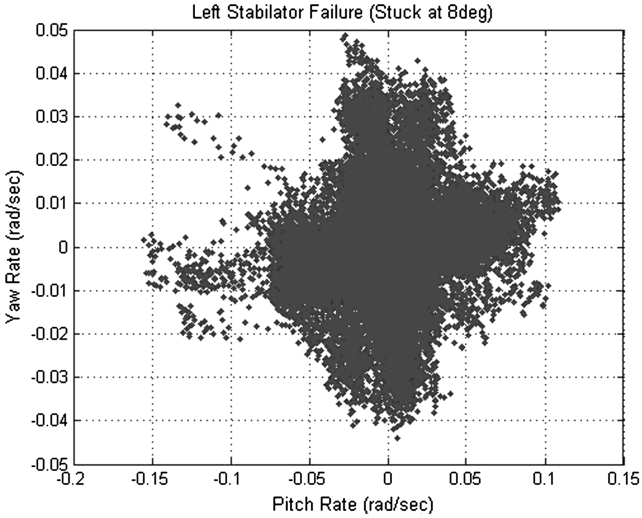

Fig. 15 **Dynamic behavior for left-stabilator failure (locked at 8 deg)**

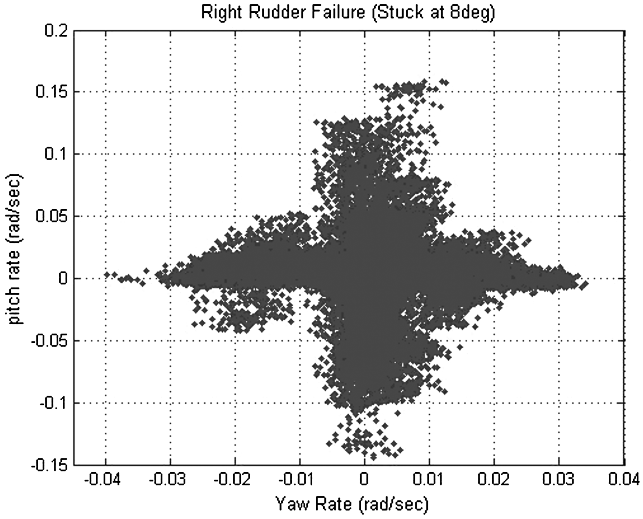

Fig. 16 **Dynamic behavior for right-rudder failure (locked at 8 deg)**

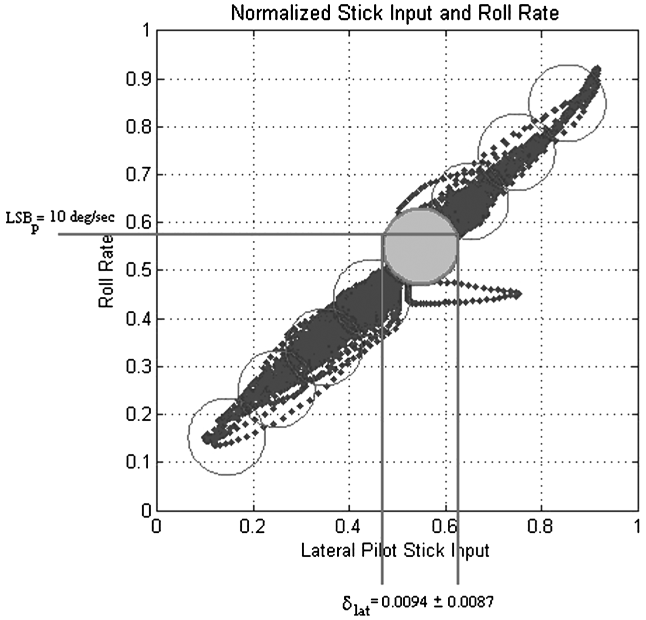

Fig. 17 **Evaluator distribution and activation when a sensor failure is declared (large step bias of the roll-rate sensor)**

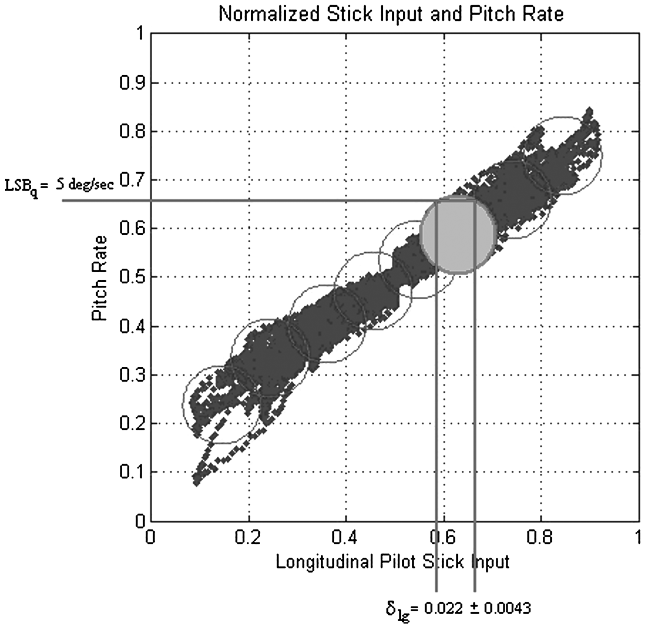

Fig. 18 **Evaluator distribution and activation when a sensor failure is declared (medium step bias of the pitch-rate sensor)**

Since the angular-rate sensors are used within the control laws of the aircraft for automatic compensation, a faulty sensor output will induce unnecessary, even damaging, compensation and may produce deflections of the aerodynamic control surfaces that are progressively closer to the saturation limit, thus limiting the stick/pedal authority of the pilot. In consequence, the stick-command inputs must represent the set of features that define the self, in such a way that when one of the three sensors fails, the estimation of the new maneuverable ranges can be performed. However, the process can also be inverted in order to estimate the achievable limits on the angular rates due to a limitation on the stick-command inputs.

The limits in nominal flight condition for the angular rates and the stick inputs are summarized in Table 12. They correspond to the maximum and minimum values of these variables that were achieved during flight test in healthy condition performed for the flight envelope described in Sec. III.

Table 12 **Nominal operational ranges**

Self variable	Minimum nominal limit	Maximum nominal limit
Roll rate	−1.19 rad/s	1.19 rad/s
Lateral stick input δ_{lat}	−0.0670 m	0.0670 m
Pitch rate	−0.25 rad/s	0.25 rad/s
Longitudinal stick input δ_{lg}	−0.0824 m	0.0824 m
Yaw rate	−0.08 rad/s	0.08 rad/s
Pedal input δ_{dir}	−0.0657 m	0.0657 m

Figures 17–19 illustrate a normalized version of the three selves with respect to the minimum and maximum nominal limits outlined in Table 12. These figures show the distribution of different sets of evaluators that have been generated for every self. Figure 17 presents the activation of an evaluator when a LSB of magnitude 10 deg/s has been identified in the roll-rate sensor. Similar examples for other magnitudes of failure are presented in Figs. 18 and 19 for pitch and yaw rate sensors, respectively. Note that the sensor failure is equivalent to a shift in the neutral position of the stick on each channel. For example, as shown in Fig. 18, a 5 deg/s step bias in the pitch-rate sensor reduces the capability of the pilot to produce a positive pitch maneuver by around 25%. In Tables 13–15 more

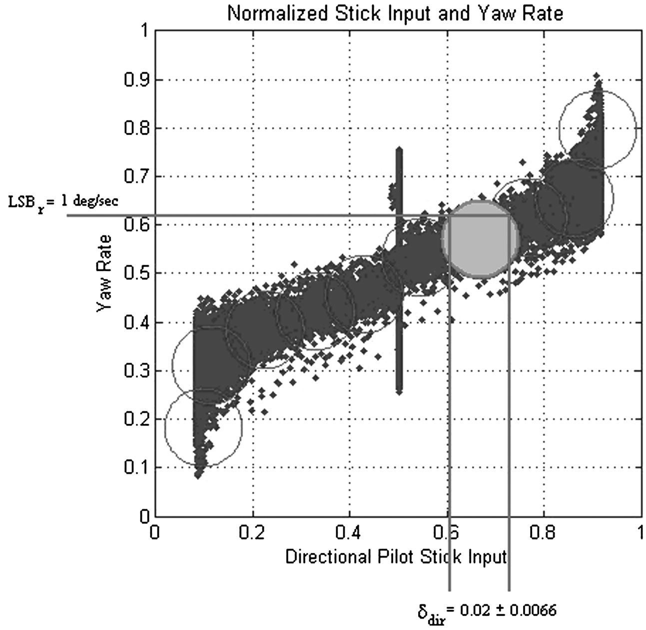

Fig. 19 Evaluator distribution and activation when a sensor failure is declared (small step bias of the yaw-rate-sensor failure)

Table 13 Effect of roll-rate-sensor failure on command-authority range: reduction percentage of capability to generate a positive roll rate

Failure type	Shift value δ_{lat}	Reduction percentage
Large step bias (10 deg/s)	0.0094 ± 0.0087	14%
Medium step bias (5 deg/s)	0.0067 ± 0.0087	10%
Small step bias (2 deg/s)	0.0040 ± 0.0087	6%

Table 14 Effect of pitch-rate-sensor failure on command-authority range: reduction percentage of capability to generate a positive pitch rate

Failure type	Shift value δ_{lg}	Reduction percentage
Large step bias (10 deg/s)	0.060 ± 0.0043	69.4%
Medium step bias (5 deg/s)	0.022 ± 0.0043	25%
Small step bias (2 deg/s)	0.010 ± 0.0086	12%

Table 15 Effect of yaw-rate-sensor failure on command-authority range: reduction percentage of capability to generate a positive yaw rate

Failure type	Shift value δ_{dir}	Reduction percentage
Large step bias (3 deg/s)	0.052 ± 0.0033	80%
Medium step bias (2 deg/s)	0.046 ± 0.0033	70%
Small step bias (1 deg/s)	0.020 ± 0.0066	30.4%

results for different magnitudes of sensor failures have been summarized.

Such results can generate offline a preliminary database that can be used for online estimation with reduced computational time. The prediction of the flight-envelope reduction when new magnitudes of failure are detected can be performed through interpolation from the offline-generated evaluators.

C. Structural Failure

To determine the effects of wing damage on aircraft performance, the aerodynamic coefficients or equivalent parameters must be considered as part of the self. The magnitude of the failure, expressed as the percentage of the wing tip removed, determines the constraints that affect the performance by reducing the lift capability. Thus, the determination of the achievable operational ranges of the damaged asymmetric aircraft is based on its current aerodynamic and structural configuration.

Note that only the aerodynamic effects associated with the loss of lift have been considered in this section. Changes in the moment coefficients, center-of-gravity shift, and aircraft mass properties may be included following the same methodology.

A simple approach based on the aerodynamic model for different wing-damage cases has been implemented. This model is used to build an offline library, and then by simple interpolation, the estimation of the lift margins can be performed online. As illustrated in Fig. 20, finite element structural models for the damaged aircraft or wind-tunnel tests can also be used to account for the damage effects and provide useful and more accurate information to the flight-envelope database.

Since the current study is focused only on single prediction of loss of lift capability, the evaluators must be generated in such a way that they express a relationship between the percentage of wing loss and the lift coefficient, and hence their activation depends on the magnitude of the damage identified by the AIS-based FDIE. Figure 21 shows the reduction of lift due to wing loss as used for the structural damage model. The lift coefficient can be reduced by as much as 18% for loss of 15% of the wingtip. Figure 22 illustrates the distribution of the evaluators generated for structural failure and the activation of one of them when a 15% of loss of the wing is present and has been identified previously by the AIS scheme. More activation results are summarized in Table 16.

As mentioned before, for the wing geometry and configuration of the F15 aircraft, a wing loss beyond 6% span will result in a deterioration of the aerodynamic efficiency of one of the ailerons. As a consequence, the asymmetrical deflection of ailerons will produce some pitch–roll coupling and a change in the lift coefficient. All of these effects have been considered in the structural damage model for both left and right wings. The evaluation approach to estimate the

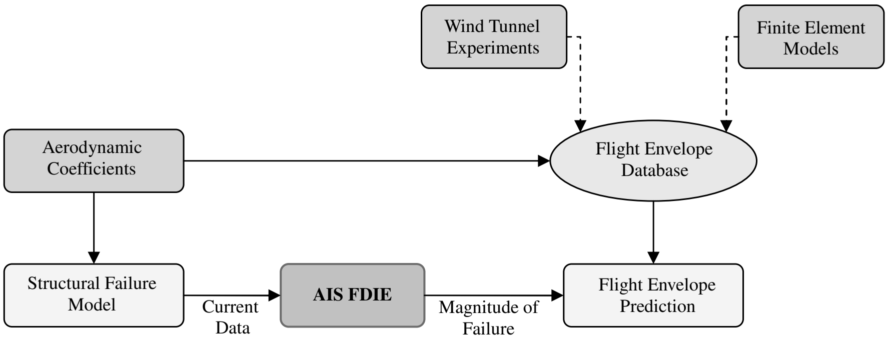

Fig. 20 Indirect evaluation scheme for structural failure

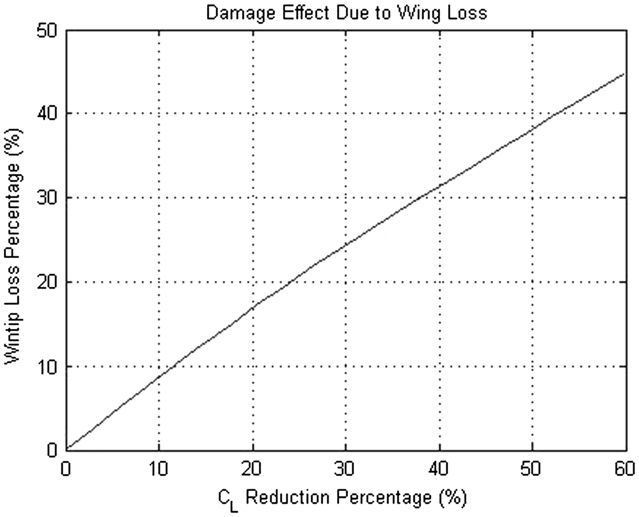

Fig. 21 Defined self for envelope reduction due to structural failure.

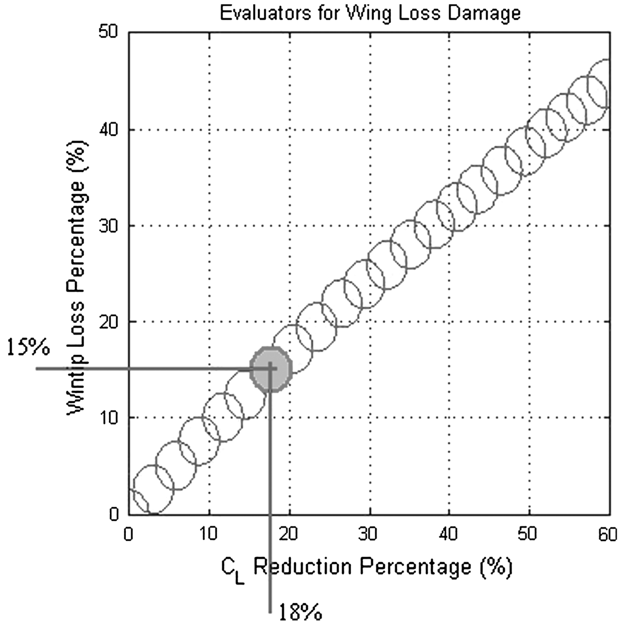

Fig. 22 Evaluator distribution and activation when a structural failure is declared.

reduction on the lift capabilities described above can be applied for both wings without any difference.

D. Engine Failure

In analyzing the effects of the propulsion-system abnormal operation, the conventional flight envelope of the F-15 ACTIVE vehicle defined in terms of airspeed and altitude [28] has been considered to be part of the feature sets that define the self. The collective power setting, calculated as the average of the power setting of the two engines, represents a set of constraints that reduce the operational ranges of the aircraft based on the achievable limits of Mach number and altitude.

Table 16 Operational ranges under structural damage

Failure type	Lift-reduction percentage
5% of loss of the right wing	6%
15% of loss of the left wing	18%
25% of loss of the right wing	30%
30% of loss of the left wing	38%

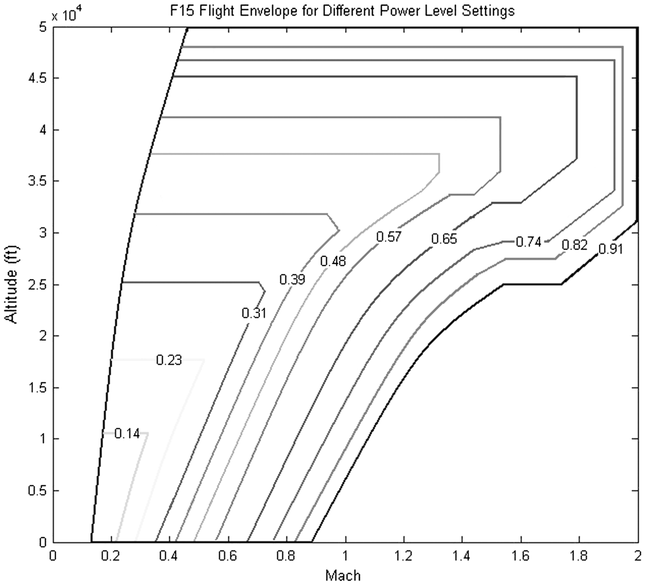

Fig. 23 F-15 flight envelope for different power settings.

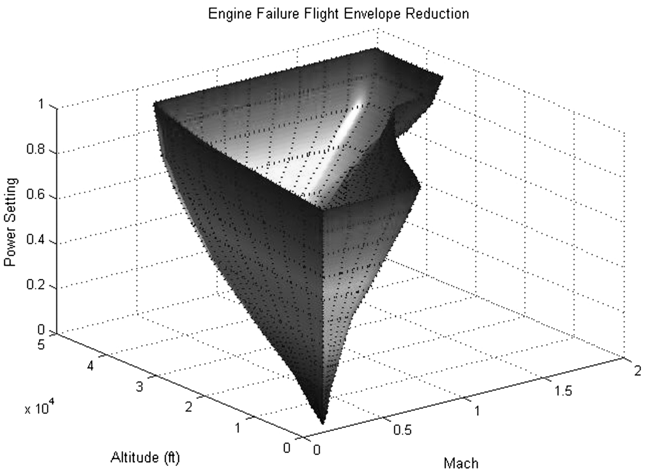

Fig. 24 Defined self for envelope-reduction prediction in the presence of propulsion failures.

As illustrated in Fig. 23, the flight-envelope areas for several power settings have been estimated. Although they represent a flight-envelope database created offline, they can be used for online estimation via interpolation using hypersphere evaluators. Figure 24 represents the defined three-dimensional self to be used for envelope-reduction prediction in the presence of propulsion-system failures.

Using positive selection, 268 hypersphere evaluators were generated. Figure 25 shows the distribution of these evaluators around the defined self regions. In this case, the set of constraints, given by the maximum and minimum values of the overall power, needs to be represented as hyperplanes intersecting the surface of the self. Then the activated evaluators will correspond to achievable limit ranges in terms of Mach and altitude for the specific failure condition.

Assuming, for example, that the right engine throttle is stuck such that the engine is producing 60% of its total power, the constrained values for the power range can be calculated as follows:

$$\delta_{T_{\max}} = \frac{\delta_{T/\text{left}_{\max}} + \delta_{T/\text{right}_{\max}}}{2} = \frac{91\% + 60\%}{2} = 75.5\% \qquad (16)$$

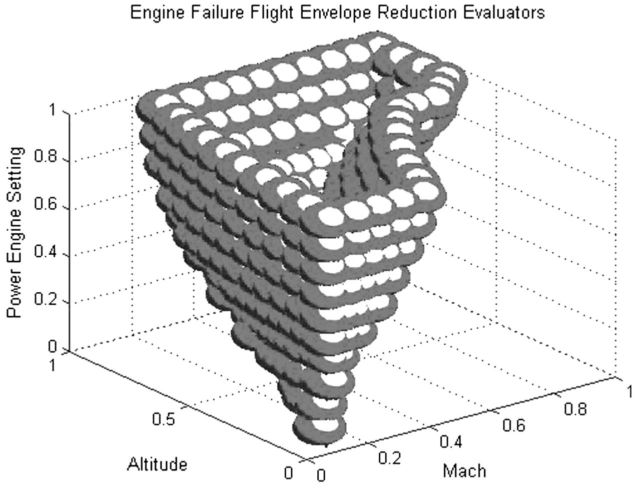

Fig. 25 Distribution of evaluators for estimation of flight-envelope reduction due to propulsion-system failure.

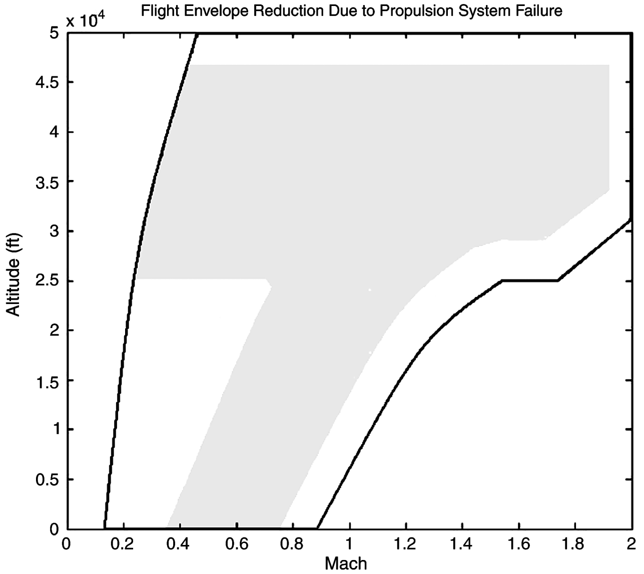

Fig. 26 Propulsion-failure impact on flight-envelope reduction (right engine stuck at 60% of its total power).

$$\delta_{T_{\min}} = \frac{\delta_{T/\mathrm{left}_{\min}} + \delta_{T/\mathrm{right}_{\min}}}{2} = \frac{0.14\% + 60\%}{2} = 30.07\% \qquad (17)$$

where $\delta_{T/\mathrm{left}_{\max}}$, $\delta_{T/\mathrm{right}_{\max}}$, $\delta_{T/\mathrm{left}_{\min}}$, and $\delta_{T/\mathrm{right}_{\min}}$ represent the maximum and minimum power settings for left and right engines.

Table 17 Flight-envelope reduction due to propulsion failures

Failure type	Mach number limits at current altitude
9000 ft	
Loss of 98% of the left power	0.18 to 0.55
Right engine power stuck at 40%	0.40 to 0.79
Left engine power stuck at 60%	0.47 to 0.90
20,000 ft	
Loss of 98% of the left power	0.23 to 0.73
Right engine power stuck at 40%	0.60 to 0.99
Left engine power stuck at 60%	0.62 to 1.17
31,000 ft	
Loss of 98% of the left power	0.33 to 1.04
Right engine power stuck at 40%	0.30 to 1.43
Left engine power stuck at 60%	0.29 to 1.79

The nominal range values for these parameters were found to be between 0.14 and 91%.

A better visualization of the reduced flight envelope can be obtained from Fig. 26. As a combination of altitude and Mach number, the dark region corresponds to the set of operational limits or achievable ranges within which the aircraft can be flown safely. In Table 17, more results for different magnitudes of failure have been summarized. The information regarding the flight-envelope reduction in this case can be provided to the pilot by displaying the limits on the Mach number at the current altitude or by displaying the altitude range for a given Mach number.

VI. Conclusions

The capabilities of the AIS-based scheme to estimate the magnitude/severity of aircraft subsystem failures (direct evaluation) and their effect on reducing the flight envelope in a general sense (indirect evaluation) have been demonstrated for several cases using data from a 6-DOF flight simulator.

The simulation study has successfully investigated and proved the feasibility of the proposed approach considering failures/damages of aircraft actuators, sensors, propulsion, and structure with different magnitudes.

The direct failure evaluation can be performed based on the distance of the nonself point with respect to the boundary of the self. This approach relies on observations of simulation data for the failure classes considered in this paper and requires further investigations to confirm and generalize.

Unlike the AIS-based FDI, the indirect failure evaluation requires algorithm customization that depends on the type of failure and the flight-envelope parameter used as criterion for the evaluation. However, the AIS paradigm has the flexibility to provide a consistent framework and achieve high performance.

Only low-dimensional flight envelopes have been considered in this study, which does not fully benefit from the capabilities of the AIS approach, especially combined with the HMS strategy, to directly address highly multidimensional problems. It is expected that future extension into considering more performance parameters will produce more compact, integrated, and global evaluation schemes.

Acknowledgments

This research effort was sponsored by NASA Aviation Safety Program through a grant within the Integrated Resilient Aircraft Control project. Special thanks to the volunteer pilots Alejandro Posada, Steven Mullins, Steven Hard, and Ondrej Karas for performing the tests in the flight simulator.

References

[1] Jones, S. M., and Reveley, M., “An Overview of the NASA Aviation Safety Program Assessment Process,” 3rd AIAA Aviation Technology, Integration, and Operations (ATIO) Conf., AIAA Paper 2003-6706, Denver, CO, Nov. 2003.

[2] Krishnakumar, K., and Gundy-Burlet, K., “Intelligent Control Approaches for Aircraft Applications,” *JANAFF Interagency Propulsion Committee Meeting*, Destin, FL, 2002.

[3] Krishnakumar, K., “Intelligent Systems For Aerospace Engineering—An Overview,” *von Karman Lecture Series on Intelligent Systems for Aeronautics*, von Karman Inst. for Fluid Dynamics, Brussels, May 2002, Paper ADA484100.

[4] Unnikrishnan, Suraj., and Prasad, J. V. R., “Reactionary Automatic Envelope Protection for Autonomous Unmanned Aerial Vehicles,” AIAA Atmospheric Flight Mechanics Conf. and Exhibit, AIAA Paper 2004-4819, Providence, RI, Aug. 2004.

[5] Unnikrishnan, S., and Prasad, J. V. R., “Carefree Handling Using Reactionary Envelope Protection Method,” AIAA Guidance, Navigation, and Control Conf., AIAA Paper 2006-6219, Keystone, CO, Aug. 2006.

[6] Tang, L., Roemer, M., Ge, J., Crassidis, A., Prasad, J. V. R., and Belcastro, C., “Methodologies for Adaptive Flight Envelope Estimation and Protection,” AIAA Guidance, Navigation, and Control Conf., AIAA Paper 2009-6260, Chicago, Aug. 2009.

[7] Keller, J., McKillip, R., and Kim, S., "Aircraft Flight Envelope Determination using Upset Detection and Physical Modeling Methods," AIAA Guidance, Navigation, and Control Conf., AIAA Paper 2009-6259, Chicago, Aug. 2009.

[8] Perhinschi, M. G., Moncayo, H., and Davis, J., "Integrated Framework for Artificial Immunity-Based Aircraft Failure Detection, Identification, and Evaluation," *Journal of Aircraft*, Vol. 47, No. 6, Nov.–Dec. 2010, pp. 1847–1859. doi:10.2514/1.45718

[9] Moncayo, H., Perhinschi, M. G., and Davis, J., "Aircraft Failure Detection and Identification Using an Immunological Hierarchical Multiself Strategy," *Journal of Guidance, Control, and Dynamics*, Vol. 33, No. 4, July–Aug. 2010, pp. 1105–1114. doi:10.2514/1.47445

[10] Dasgupta, D., and Forrest, S., "Artificial Immune Systems in Industrial Applications," *Proceedings of the Second International Conference on Intelligent Processing and Manufacturing of Materials*, IEEE Press, Piscataway, NJ, 1999, pp. 257–267.

[11] Dasgupta, D., Krishnakumar, K., Wong, D., and Berry, M., "Negative Selection Algorithm for Aircraft Fault Detection," *Lecture Notes in Computer Science*, Vol. 3239/2004, 2004, pp. 1–23. doi:10.1007/978-3-540-30220-9_1

[12] Krishnakumar, K., "Artificial Immune System Approaches for Aerospace Applications," 41st Aerospace Sciences Meeting & Exhibit, AIAA Paper 2003-0457, Reno, NV, 2003.

[13] Benjamini, E., *Immunology, A Short Course*, Wiley-Liss, New York, 1992.

[14] Forrest, S., Perelson, A. S., Allen, L., and Cherukuri, R., "Self–Nonself Discrimination in a Computer," *Proceedings of the IEEE Symposium on Research in Security and Privacy*, IEEE Computer Society Press, Los Alamitos, CA, 1994, pp. 202–212.

[15] Dasgupta, D., and Majumdar, N., "Anomaly Detection in Multidimensional Data Using Negative Selection Algorithm," *Proceedings of the Congress on Evolutionary Computation CEC '02*, Vol. 2, 2002, pp. 1039–1044.

[16] Gonzalez, F., and Dasgupta, D., "Anomaly Detection Using Real-Valued Negative Selection," *Genetic Programming and Evolvable Machines*, Vol. 4, No. 4, 2003, pp. 383–403. doi:10.1023/A:1026195112518

[17] Gonzalez, F., Dasgupta, D., and Niño, L., "A Randomized Real-Valued Negative Selection Algorithm," *Proceedings of the 2nd International Conference on Artificial Immune Systems*, Edinburgh, Scotland, U.K., 2003, pp. 261–272.

[18] Stibor, T., Timmis, J., and Eckert, C., "On the Appropriateness of Negative Selection Defined over Hamming Shape-Space as a Network Intrusion Detection System," *Proceedings of the 4th International Conference on Artificial Immune Systems*, 2006.

[19] Sanchez, S. P., Perhinschi, M. G., Moncayo, H., Napolitano, M. R., Davis, J., and Fravolini, M. L., "In-Flight Actuator Failure Detection and Identification for a Reduced Size UAV Using the Artificial Immune System Approach," AIAA Guidance, Navigation, and Control Conf., AIAA Paper 2009-6266, Chicago, Aug. 2009.

[20] Perhinschi, M. G., Campa, G., Napolitano, M. R., Lando, M., Massotti, L., and Fravolini, M. L., "Modeling and Simulation of a Fault Tolerant Control System," *International Journal of Modelling and Simulation*, Vol. 26, No. 1, Jan. 2006, pp. 1–10. doi:10.2316/Journal.205.2006.1.205-4044

[21] Antoniewicz, R. F., Duke, E. L., and Patterson, B. P., "User's Manual for Interactive LINEAR, a Fortran Program to Derive Linear Aircraft Models," NASA TP 2835, 1988.

[22] Perhinschi, M. G., and Napolitano, M. R., "A Simulation Environment for Design and Testing of Aircraft Adaptive Fault-Tolerant Control Systems," *Aircraft Engineering and Aerospace Technology*, Vol. 80, No. 6, Dec. 2008, pp. 620–632. doi:10.1108/00022660810911563

[23] Perhinschi, M. G., Napolitano, M. R., Campa, G., Fravolini, M. L., and Seanor, B., "Integration of Sensor and Actuator Failure Detection, Identification, and Accommodation Schemes Within Fault Tolerant Control Laws," *Control and Intelligent Systems*, Vol. 35, No. 4, Dec. 2007, pp. 309–318. doi:10.2316/Journal.201.2007.4.201-1657

[24] Perhinschi, M. G., Napolitano, M. R., Campa, G., and Fravolini, M. L., "A Simulation Environment for Testing And Research of Neurally Augmented Fault Tolerant Control Laws Based on Non-Linear Dynamic Inversion," AIAA Modeling and Simulation Technologies Conf., AIAA Paper 2004-4913, Providence RI, 2004.

[25] Perhinschi, M. G., Napolitano, M. R., Campa, G., Seanor, B., and Gururajan, S., "Design of Intelligent Flight Control Laws for the WVU F-22 Model Aircraft," AIAA Intelligent Systems Technical Conf., AIAA Paper 2004-6282, Chicago, 2004.

[26] Perhinschi, M. G., Napolitano, M. R., Campa, G., Seanor, B., Burken, J., and Larson, R., "An Adaptive Threshold Approach for the Design of an Actuator Failure Detection and Identification Scheme," *IEEE Transactions on Control Systems Technology*, Vol. 14, No. 3, May 2006, pp. 519–525. doi:10.1109/TCST.2005.860522

[27] Davis, J., Perhinschi, M. G., and Moncayo, H., "Evolutionary Algorithm for Artificial-Immune-System-Based Failure-Detector Generation and Optimization," *Journal of Guidance, Control, and Dynamics*, Vol. 33, No. 2, March–April 2010, pp. 305–320. doi:10.2514/1.46126

[28] Conners, T. R., and Sims, R. L., "Full Flight Envelope Direct Thrust Measurement on a Supersonic Aircraft," NASA Dryden Flight Research Center, TM-1998-206560, Edwards AFB, CA, July 1998.